Cite as: H. Reddy *et al.*, *Science* 10.1126/science.abb3457 (2020).

Determining plasmonic hot-carrier energy distributions via single-molecule transport measurements

Harsha Reddy[1]*, Kun Wang[2]*, Zhaxylyk Kudyshev[1,3], Linxiao Zhu[2], Shen Yan[2], Andrea Vezzoli[4], Simon J. Higgins[4], Vikram Gavini[2,5], Alexandra Boltasseva[1], Pramod Reddy[2,5]†, Vladimir M. Shalaev[1]†, Edgar Meyhofer[2]†

[1]School of Electrical and Computer Engineering, Purdue University, West Lafayette, IN 47907, USA. [2]Department of Mechanical Engineering, University of Michigan, Ann Arbor, MI 48109, USA. [3]Center for Science of Information, Purdue University, West Lafayette, IN 47907, USA. [4]Department of Chemistry, University of Liverpool, Liverpool L69 7ZD, UK. [5]Department of Materials Science and Engineering, University of Michigan, Ann Arbor, MI 48109, USA.

*These authors contributed equally to this work.

†Corresponding author. Email: pramodr@umich.edu (P.R.); shalaev@purdue.edu (V.M.S.); meyhofer@umich.edu (E.M.)

Hot-carriers in plasmonic nanostructures, generated via plasmon decay, play key roles in applications like photocatalysis and in photodetectors that circumvent band-gap limitations. However, direct experimental quantification of steady-state energy distributions of hot-carriers in nanostructures has so far been lacking. We present transport measurements from single-molecule junctions, created by trapping suitably chosen single molecules between an ultra-thin gold film supporting surface plasmon polaritons and a scanning probe tip, that can provide quantification of plasmonic hot-carrier distributions. Our results show that Landau damping is the dominant physical mechanism of hot-carrier generation in nanoscale systems with strong confinement. The technique developed in this work will enable quantification of plasmonic hot-carrier distributions in nanophotonic and plasmonic devices.

Hot-carriers, energetic electrons and holes with energy distributions that deviate significantly from equilibrium Fermi-Dirac distributions (*1*), are expected to arise in metallic nanostructures due to the non-radiative decay of surface plasmons. Such hot-carriers hold promise for the development of a variety of technologies, including plasmon-driven photochemistry (*2–5*), alternative solar-energy harvesting devices (*6*), and efficient photodetectors operating below bandgap (*7–9*). Central to the design and development of these applications is knowledge of the hot-carrier energy distributions (HCEDs) that are generated under steady-state conditions (*10*). While past work has tried to quantify HCEDs (*11–15*), a majority of this work has relied on first-principle calculations or semi-classical approaches, which involve assumptions on the dominant relaxation pathways of hot-carriers as well as material properties (*15*) that lead to significant uncertainties in the estimated HCEDs (*12*, *13*). In fact, recent calculations (*16*) have even suggested that the deviations from the equilibrium Fermi-Dirac distribution are negligibly small, questioning past calculations. Therefore, direct experimental observations are critical for obtaining detailed insights into the HCEDs and for rationally engineering the aforementioned technologies.

Here, we show how scanning probe-based techniques (*17–19*) that measure charge transport in single molecules, when combined with nanoplasmonic experimental methods, can be leveraged to directly quantify steady-state HCEDs [$f_{hot}(E)$] in a key model system—a thin gold film that supports propagating surface plasmon polaritons (SPPs). Our basic strategy is to first create single-molecule junctions (SMJs)—using carefully chosen molecules with appropriate transmission characteristics—between a plasmonic gold (Au) film and the Au tip of a scanning tunneling microscope (STM), and elucidate the current-voltage characteristics with and without plasmonic excitation at various voltage biases (V_{bias}) (see Fig. 1A). The difference in the measured currents for the cases with [$I_{SPP}(V_{bias})$] and without [$I_d(V_{bias})$] plasmonic excitation, which we call the hot-carrier current $I_{hot}(V_{bias}) = I_{SPP}(V_{bias}) - I_d(V_{bias})$, enables us to directly quantify $f_{hot}(E)$.

To elaborate, as depicted in Fig. 1, B and C, $I_{hot}(V_{bias})$ arises due to the generation of the non-equilibrium carriers under plasmonic excitation with an energy distribution $f_{ne}(E)$. We note that the energy distribution $f_{hot}(E)$ represents the difference between $f_{ne}(E)$ and the equilibrium Fermi-Dirac distribution $f_{eq}(E)$ as $f_{hot}(E) = f_{ne}(E) - f_{eq}(E)$. As explained in detail in the supplementary materials (*20*), $f_{hot}(E)$ and $I_{hot}(V_{bias})$ are related by

$$I_{hot}(V_{bias}) = \frac{2e}{h}\int_{-\infty}^{\infty} T(E) f_{hot}\left(E - \frac{eV_{bias}}{2}\right) dE \qquad (1)$$

where $T(E)$ is the transmission function of the SMJ, e is the elemental charge and h is the Planck constant. When SMJs that feature a sharp peak in $T(E)$ are employed, $I_{hot}(V_{bias})$ is predominantly determined by the hot-carriers with energies close to the transmission peak, simplifying the above integral to [(*20*), section 1]

$$I_{hot}(V_{bias}) \approx \frac{2e}{h} f_{hot}\left(E_0 - \frac{eV_{bias}}{2}\right)\int_{-\infty}^{\infty} T(E)\,dE \qquad (2)$$

where E_0 is the energy of the peak in $T(E)$. Equation 2 relates $I_{hot}(V_{bias})$ to $f_{hot}(E)$ via a voltage- and energy-independent constant scaling factor $\left(\frac{2e}{h}\int_{-\infty}^{\infty} T(E)\,dE\right)$. Therefore, by varying V_{bias} in the window $\{V_0{:}-V_0\}$, the steady-state HCEDs can be mapped within the energy window $\left\{E_0 - \frac{eV_0}{2} : E_0 + \frac{eV_0}{2}\right\}$ (Fig. 1C).

We used the molecules shown in Fig. 1D (labeled ***L1***, ***H1***, ***L2***) for experimental quantification of the HCEDs. Molecule ***L1*** represents a charge-transfer complex of quaterthiophene (T4) and tetracyanoethylene (TCNE) with terminal thiophenes containing gold-binding methyl sulfides, while the ***H1*** molecule, 3,4-ethylenedioxythiophene (EDOT), is flanked by two thiophenes with terminal thiophenes containing gold-binding methyl sulfides. The transmission characteristics of Au-***L1***-Au and Au-***H1***-Au SMJs are expected to be sharply peaked and dominated by the lowest unoccupied molecular orbital (LUMO) (*21*, *22*) and highest occupied molecular orbital (HOMO) (*23*), respectively. Finally, we also utilize ***L2***, 1,4-benzenediisonitrile molecules [see section 3 of (*20*) for additional details], SMJs created from which are expected to feature weakly energy-dependent $T(E)$ also dominated by the LUMO level (*24*).

Plasmonic gold films (thickness 6 nm and 13 nm), with integrated grating couplers, were fabricated on fused silica substrates (Fig. 1A) to excite SPPs and generate hot-carriers [(*20*), section 4]. The 6 nm-thick gold film with grating coupler was first exposed to a solution containing ***L1*** molecules to create a monolayer of the molecules [(*20*), section 5]. Next, we positioned a Au STM tip at a separation of ~1 μm (along the x direction) from the grating edge (fig. S2). Subsequently, the Au film was covered with an immersion oil matching the refractive index of fused silica to create a symmetric optical medium around the film, and a V_{bias} = 0.1 V was applied to the STM tip while grounding the Au film. We then employed the STM break-junction technique (*17*, *18*) [see (*20*), section 2 for a detailed protocol] to identify the current through a Au-***L1***-Au SMJ. The peak in the current histogram created from over 2000 current vs. displacement traces represents the most probable current (I_d)—corresponding to a conductance of 8.5×10^{-4} G_0 for a Au-***L1***-Au junction (Fig. 2A) under the absence of plasmonic excitation [$G_0 \approx (12.9\ k\Omega)^{-1}$ is the quantum of electrical conductance], in good agreement with prior work (*22*). Subsequently, we illuminated the gratings with a focused 830 nm, linearly polarized laser beam (0.3 mW/μm^2 power density) perpendicular to the grating strips, launching SPPs in the Au film (Fig. 1A). Concurrently, we measured the electrical current and found that the most probable current I_{SPP} is larger than I_d (Fig. 2A). We then determined the hot-carrier current as $I_{hot}(V_{bias} = 0.1\ V) = I_{SPP}(V_{bias} = 0.1\ V) - I_d(V_{bias} = 0.1\ V)$. The measured $I_{hot}(V_{bias} = 0.1\ V)$ displayed a strong dependence on the laser polarization (Fig. 2C), consistent with the polarization dependent SPP excitation efficiency, indicating that the measured I_{hot} is due to the excitation of SPPs. Additional control experiments further confirmed that the measured I_{hot} is indeed due to hot-carrier effects and not due to an increased temperature or simple light-assisted transport [(*20*), section 6].

Next, we performed additional measurements from Au-***L1***-Au SMJs at the same location, while varying V_{bias} from {−0.3 V:0.3 V}. The measured bias-dependent $I_{hot}(V_{bias})$ (fig. S16A) displayed an asymmetric shape with a peak around 0.15 V. Further, the transmission characteristics of Au-***L1***-Au junctions, necessary for determining the spectral distribution of hot carriers (see Eqs. 1 and 2), were obtained using an experimental approach developed in (*23*) [(*20*), section 7]. Figure 2D shows the $T(E)$ obtained for Au-***L1***-Au junctions. Consistent with past work (*23*), we fit the measured $T(E)$ with a Lorentzian and obtained the energy of the peak to be $E_0 \approx$ 0.18 eV relative to the Fermi energy (E_F) with a peak width of 2.6 meV (Fig. 2D), confirming the sharp nature of the peak [(*20*), section 7], in good agreement with past computational work (*22*). Subsequently, we determined $f_{hot}(E)$ from the measured $I_{hot}(V_{bias})$ and $T(E)$ of ***L1*** using Eq. 2. The measured $f_{hot}(E)$ (see Fig. 3A) revealed the relative hot-electron energy distribution (HEED), displaying a peak around 100 meV followed by a decaying tail extending up to about 330 meV above E_F. It should be noted that, as the transmission function peak enters the window between the quasi Fermi levels of the two contacts, extremely large currents flow through the molecular junction making the junction unstable and limiting the V_{bias} sweep window to {−0.3 V:0.3 V} and the energy window to {0.03 eV:0.33 eV} with respect to E_F [(*20*), section 7]. However, this is not a fundamental limitation as additional measurements and analysis with Au-***L2***-Au SMJs enabled measurements of the HEED at higher energies, which revealed that there are negligibly few hot-electrons with energies beyond 0.4 eV [dashed line in the inset of Fig. 3A, (*20*), section 10].

To determine the hot-hole energy distribution (HHED), i.e., energies below E_F, we repeated measurements of $I_{hot}(V_{bias})$ in Au-***H1***-Au SMJs for V_{bias} in the range of {−1.5 V:1 V} (fig. S16B). Unlike for ***L1***, where large $I_{hot}(V_{bias})$ was observed for positive V_{bias}, no perceptible $I_{hot}(V_{bias})$ was recorded in ***H1*** junctions for positive V_{bias}. Instead, $I_{hot}(V_{bias})$ in ***H1*** junctions increased above the noise floor for V_{bias} below −0.6 V and peaked around −1.2 V. Next, we measured the transmission characteristics of Au-***H1***-Au junctions, and obtained the Lorentzian-shaped transmission characteristics shown in

Fig. 2E, which features a peak at $E_0 \approx -0.7$ eV and a peak width of 6.8 meV, in good agreement with prior work (*23*). From the measured $T(E)$ and $I_{hot}(V_{bias})$, we obtained $f_{hot}(E)$ using Eq. 2 over the energy range {−1.2 eV:0.05 eV} (Fig. 3B). The HHED featured a peak around −0.1 eV and a decaying tail that extends to energies about −0.4 eV with respect to E_F.

To gain insights into the microscopic origin of our observations, we performed first-principle density functional theory (DFT) calculations (*11*) to compute the hot-carrier generation rates and subsequently employed the Boltzmann transport equation under the relaxation time approximation (*25*) to obtain the steady-state HCEDs [(*20*), section 11]. For our calculations, we considered a geometry consisting of a Au film surrounded by a symmetric dielectric environment with a refractive index $n = 1.45$, mimicking the geometry in our experiments, which is known to support two plasmonic modes: a symmetric mode and an antisymmetric mode with distinct dispersion relations (*26*–*28*).

The computed HCED arising from the symmetric plasmonic mode on a 6 nm-thick Au film, obtained using both an energy-dependent electron-electron collision rate from Landau's Fermi liquid theory (FLT) (*29*) and an energy-independent scattering rate are shown in Fig. 4A. Additionally, electron-phonon scattering is included via an energy-independent relaxation rate (*30*). Note that these computational results are multiplied by a scaling factor so that the peak value is 1. The results obtained following FLT predict that hot-carriers are largely populated within the energy window of {−0.4 V:0.4 V} relative to E_F—in excellent agreement with our experiments. In contrast, an energy-independent scattering rate results in hot-carriers in a larger range of energies (Fig. 4A, blue curve) that disagree with our experimental observations. These findings establish the validity of employing the energy-dependent electron-electron collision rate for modelling hot-carriers in plasmonic nanostructures.

To understand the effect of film thickness we measured the HCED in thicker (13 nm-thick) Au films. The measured HCED (Fig. 3, C and D) showed that the hot-carriers are mostly populated around E_F. Besides, the total number of hot-carriers $\left(\int_{E_F-\hbar\omega}^{E_F+\hbar\omega} |f_{hot}(E)| dE\right)$ was found to be ~40% smaller than those measured on 6 nm film. The observed reduction in the magnitude of HCED in thicker films can be attributed to the effect of surface-assisted absorption—Landau damping (*13*, *15*, *25*) [see relevant discussion in (*20*), section 11]. To quantify the role of Landau damping, we computed the HCED in a 13 nm film arising from the symmetric plasmonic mode, and electron-electron scattering rates from FLT (Fig. 4A), which revealed that the generated hot-carriers are populated close to E_F, similar to the 6 nm film. However, about 43% fewer hot-carriers are generated in the 13 nm film, in good agreement with our experiments.

To elucidate the distance-dependence of hot-carrier generation, we measured I_{hot} for Au-***L1***-Au SMJs at $V_{bias} = 0.1$ V for varying separations (d) from the grating edge on a 6 nm-thick gold film [see Fig. 4C and (*20*), section 14]. The measured I_{hot} decreases as the separation from the edge of the gratings increases and drops close to zero for $d > 7.5$ μm. To understand the observed distance-dependence, we simulated (using the Lumerical FDTD package) the intensity profile in the 6 nm film upon illuminating the grating coupler with an 830 nm laser. A beating profile was observed close to the gratings (Fig. 4D), which we attribute to the interference between the two plasmonic modes [(*20*), section 13 and inset in Fig. 4D]. However, for $d > 10$ μm the symmetric mode decays while the antisymmetric mode shows very little decay. Since there are no observed hot-carriers at large separations, despite the presence of the antisymmetric mode, we conclude that the contribution of the antisymmetric mode to hot-electron generation is negligible. Additional calculations (Fig. 4B) confirmed that the antisymmetric mode is indeed much less effective in generating hot-electrons, resulting in 400-times (30-times) fewer carriers, in comparison to the symmetric mode for the 6 nm (13 nm)-thick film.

Our scanning probe-based approach combines single-molecule quantum transport measurements and nanoplasmonics to directly map the steady-state energy distributions of hot-carriers. The approaches developed will enable fundamental insights into hot-carrier generation processes and are critical for future hot-carrier assisted technologies.

REFERENCES AND NOTES

1. J. M. Ziman, *Principles of the Theory of Solids* (Cambridge Univ. Press, ed. 2, 1972).
2. S. Linic, P. Christopher, D. B. Ingram, Plasmonic-metal nanostructures for efficient conversion of solar to chemical energy. *Nat. Mater.* **10**, 911–921 (2011). doi:10.1038/nmat3151 Medline
3. S. Linic, U. Aslam, C. Boerigter, M. Morabito, Photochemical transformations on plasmonic metal nanoparticles. *Nat. Mater.* **14**, 567–576 (2015). doi:10.1038/nmat4281 Medline
4. L. Zhou, D. F. Swearer, C. Zhang, H. Robatjazi, H. Zhao, L. Henderson, L. Dong, P. Christopher, E. A. Carter, P. Nordlander, N. J. Halas, Quantifying hot carrier and thermal contributions in plasmonic photocatalysis. *Science* **362**, 69–72 (2018). doi:10.1126/science.aat6967 Medline
5. A. Naldoni, F. Riboni, U. Guler, A. Boltasseva, V. M. Shalaev, A. V. Kildishev, Solar-powered plasmon-enhanced heterogeneous catalysis. *Nanophotonics* **5**, 112–133 (2016). doi:10.1515/nanoph-2016-0018
6. C. Clavero, Plasmon-induced hot-electron generation at nanoparticle/metal-oxide interfaces for photovoltaic and photocatalytic devices. *Nat. Photonics* **8**, 95–103 (2014). doi:10.1038/nphoton.2013.238
7. M. W. Knight, H. Sobhani, P. Nordlander, N. J. Halas, Photodetection with active optical antennas. *Science* **332**, 702–704 (2011). doi:10.1126/science.1203056 Medline
8. H. Chalabi, D. Schoen, M. L. Brongersma, Hot-electron photodetection with a plasmonic nanostripe antenna. *Nano Lett.* **14**, 1374–1380 (2014). doi:10.1021/nl4044373 Medline
9. A. Sobhani, M. W. Knight, Y. Wang, B. Zheng, N. S. King, L. V. Brown, Z. Fang, P. Nordlander, N. J. Halas, Narrowband photodetection in the near-infrared with a plasmon-induced hot electron device. *Nat. Commun.* **4**, 1643 (2013). doi:10.1038/ncomms2642 Medline

10. A. O. Govorov, H. Zhang, Y. K. Gun'ko, Theory of photoinjection of hot plasmonic carriers from metal nanostructures into semiconductors and surface molecules. *J. Phys. Chem. C* **117**, 16616–16631 (2013). doi:10.1021/jp405430m
11. R. Sundararaman, P. Narang, A. S. Jermyn, W. A. Goddard 3rd, H. A. Atwater, Theoretical predictions for hot-carrier generation from surface plasmon decay. *Nat. Commun.* **5**, 5788 (2014). doi:10.1038/ncomms6788 Medline
12. A. Manjavacas, J. G. Liu, V. Kulkarni, P. Nordlander, Plasmon-induced hot carriers in metallic nanoparticles. *ACS Nano* **8**, 7630–7638 (2014). doi:10.1021/nn502445f Medline
13. H. Zhang, A. O. Govorov, Optical generation of hot plasmonic carriers in metal nanocrystals: The effects of shape and field enhancement. *J. Phys. Chem. C* **118**, 7606–7614 (2014). doi:10.1021/jp500009k
14. T. Heilpern, M. Manjare, A. O. Govorov, G. P. Wiederrecht, S. K. Gray, H. Harutyunyan, Determination of hot carrier energy distributions from inversion of ultrafast pump-probe reflectivity measurements. *Nat. Commun.* **9**, 1853 (2018). doi:10.1038/s41467-018-04289-3 Medline
15. J. B. Khurgin, Hot carriers generated by plasmons: Where are they generated and where do they go from there? *Faraday Discuss.* **214**, 35–58 (2019). doi:10.1039/C8FD00200B Medline
16. Y. Dubi, Y. Sivan, "Hot" electrons in metallic nanostructures-non-thermal carriers or heating? *Light Sci. Appl.* **8**, 89 (2019). doi:10.1038/s41377-019-0199-x Medline
17. B. Xu, N. J. Tao, Measurement of single-molecule resistance by repeated formation of molecular junctions. *Science* **301**, 1221–1223 (2003). doi:10.1126/science.1087481 Medline
18. P. Reddy, S.-Y. Jang, R. A. Segalman, A. Majumdar, Thermoelectricity in molecular junctions. *Science* **315**, 1568–1571 (2007). doi:10.1126/science.1137149 Medline
19. L. Cui, W. Jeong, S. Hur, M. Matt, J. C. Klöckner, F. Pauly, P. Nielaba, J. C. Cuevas, E. Meyhofer, P. Reddy, Quantized thermal transport in single-atom junctions. *Science* **355**, 1192–1195 (2017). doi:10.1126/science.aam6622 Medline
20. See supplementary materials.
21. A. Vezzoli, I. Grace, C. Brooke, K. Wang, C. J. Lambert, B. Xu, R. J. Nichols, S. J. Higgins, Gating of single molecule junction conductance by charge transfer complex formation. *Nanoscale* **7**, 18949–18955 (2015). doi:10.1039/C5NR04420K Medline
22. K. Wang, A. Vezzoli, I. M. Grace, M. McLaughlin, R. J. Nichols, B. Xu, C. J. Lambert, S. J. Higgins, Charge transfer complexation boosts molecular conductance through Fermi level pinning. *Chem. Sci.* **10**, 2396–2403 (2019). doi:10.1039/C8SC04199G Medline
23. B. Capozzi, J. Z. Low, J. Xia, Z. F. Liu, J. B. Neaton, L. M. Campos, L. Venkataraman, Mapping the transmission functions of single-molecule junctions. *Nano Lett.* **16**, 3949–3954 (2016). doi:10.1021/acs.nanolett.6b01592 Medline
24. W. Lee, K. Kim, W. Jeong, L. A. Zotti, F. Pauly, J. C. Cuevas, P. Reddy, Heat dissipation in atomic-scale junctions. *Nature* **498**, 209–212 (2013). doi:10.1038/nature12183 Medline
25. L. V. Besteiro, X. T. Kong, Z. Wang, G. Hartland, A. O. Govorov, Understanding hot-electron generation and plasmon relaxation in metal nanocrystals: Quantum and classical mechanisms. *ACS Photonics* **4**, 2759–2781 (2017). doi:10.1021/acsphotonics.7b00751
26. S. Bozhevolnyi, *Plasmonic Nanoguides and Circuits* (Pan Stanford Publishing, 2009).
27. P. Berini, Long-range surface plasmon polaritons. *Adv. Opt. Photonics* **1**, 484–588 (2009). doi:10.1364/AOP.1.000484
28. A. V. Zayats, S. A. Maier, *Active Plasmonics and Tuneable Plasmonic Metamaterials* (Wiley, 2013).
29. P. Coleman, *Introduction to Many-Body Physics* (Cambridge Univ. Press, 2015).
30. R. H. M. Groeneveld, R. Sprik, A. Lagendijk, Femtosecond spectroscopy of electron-electron and electron-phonon energy relaxation in Ag and Au. *Phys. Rev. B* **51**, 11433–11445 (1995). doi:10.1103/PhysRevB.51.11433 Medline
31. S. Datta, *Electronic Transport in Mesoscopic Systems* (Cambridge Univ. Press, 1995).
32. J. J. Apperloo, L. B. Groenendaal, H. Verheyen, M. Jayakannan, R. A. J. Janssen, A. Dkhissi, D. Beljonne, R. Lazzaroni, J.-L. Brédas, Optical and redox properties of a series of 3,4-ethylenedioxythiophene oligomers. *Chemistry* **8**, 2384–2396 (2002). doi:10.1002/1521-3765(20020517)8:10<2384:AID-CHEM2384>3.0.CO;2-L Medline
33. J. B. Khurgin, How to deal with the loss in plasmonics and metamaterials. *Nat. Nanotechnol.* **10**, 2–6 (2015). doi:10.1038/nnano.2014.310 Medline
34. G. V. Hartland, L. V. Besteiro, P. Johns, A. O. Govorov, What's so hot about electrons in metal nanoparticles? *ACS Energy Lett.* **2**, 1641–1653 (2017). doi:10.1021/acsenergylett.7b00333
35. I. Doron-Mor, Z. Barkay, N. Filip-Granit, A. Vaskevich, I. Rubinstein, Ultrathin gold island films on silanized glass. Morphology and optical properties. *Chem. Mater.* **16**, 3476–3483 (2004). doi:10.1021/cm049605a
36. T. Karakouz, D. Holder, M. Goomanovsky, A. Vaskevich, I. Rubinstein, Morphology and refractive index sensitivity of gold island films. *Chem. Mater.* **21**, 5875–5885 (2009). doi:10.1021/cm902676d
37. A. Kossoy, V. Merk, D. Simakov, K. Leosson, S. Kéna-Cohen, S. A. Maier, Optical and structural properties of ultra-thin gold films. *Adv. Opt. Mater.* **3**, 71–77 (2015). doi:10.1002/adom.201400345
38. M. Hu, S. Noda, T. Okubo, Y. Yamaguchi, H. Komiyama, Structure and morphology of self-assembled 3-mercaptopropyltrimethoxysilane layers on silicon oxide. *Appl. Surf. Sci.* **181**, 307–316 (2001). doi:10.1016/S0169-4332(01)00399-3
39. C. A. Goss, D. H. Charych, M. Majda, Application of (3-mercaptopropyl)trimethoxysilane as a molecular adhesive in the fabrication of vapor-deposited gold electrodes on glass substrates. *Anal. Chem.* **63**, 85–88 (1991). doi:10.1021/ac00001a018
40. B. Ren, G. Picardi, B. Pettinger, Preparation of gold tips suitable for tip-enhanced Raman spectroscopy and light emission by electrochemical etching. *Rev. Sci. Instrum.* **75**, 837–841 (2004). doi:10.1063/1.1688442
41. L. Cui, R. Miao, C. Jiang, E. Meyhofer, P. Reddy, Perspective: Thermal and thermoelectric transport in molecular junctions. *J. Chem. Phys.* **146**, 092201 (2017). doi:10.1063/1.4976982
42. B. Capozzi, J. Xia, O. Adak, E. J. Dell, Z. F. Liu, J. C. Taylor, J. B. Neaton, L. M. Campos, L. Venkataraman, Single-molecule diodes with high rectification ratios through environmental control. *Nat. Nanotechnol.* **10**, 522–527 (2015). doi:10.1038/nnano.2015.97 Medline
43. A. Archambault, F. Marquier, J.-J. Greffet, C. Arnold, Quantum theory of spontaneous and stimulated emission of surface plasmons. *Phys. Rev. B* **82**, 035411 (2010). doi:10.1103/PhysRevB.82.035411
44. A. D. Rakić, A. B. Djurišić, J. M. Elazar, M. L. Majewski, Optical properties of metallic films for vertical-cavity optoelectronic devices. *Appl. Opt.* **37**, 5271–5283 (1998). doi:10.1364/AO.37.005271 Medline
45. R. Sundararaman, K. Letchworth-Weaver, K. A. Schwarz, D. Gunceler, Y. Ozhabes, T. A. Arias, JDFTx: Software for joint density-functional theory. *SoftwareX* **6**, 278–284 (2017). doi:10.1016/j.softx.2017.10.006 Medline
46. J. P. Perdew, A. Ruzsinszky, G. I. Csonka, O. A. Vydrov, G. E. Scuseria, L. A. Constantin, X. Zhou, K. Burke, Restoring the density-gradient expansion for exchange in solids and surfaces. *Phys. Rev. Lett.* **100**, 136406 (2008). doi:10.1103/PhysRevLett.100.136406 Medline
47. S. L. Dudarev, G. A. Botton, A. Y. Savrasov, C. J. Humphreys, A. P. Sutton, Electron-energy-loss spectra and the structural stability of nickel oxide: An LSDA+U study. *Phys. Rev. B* **57**, 1505–1509 (1998). doi:10.1103/PhysRevB.57.1505
48. N. Marzari, D. Vanderbilt, Maximally localized generalized Wannier functions for composite energy bands. *Phys. Rev. B* **56**, 12847–12865 (1997). doi:10.1103/PhysRevB.56.12847
49. I. Souza, N. Marzari, D. Vanderbilt, Maximally localized Wannier functions for entangled energy bands. *Phys. Rev. B* **65**, 035109 (2001). doi:10.1103/PhysRevB.65.035109
50. M. Lundstrom, *Fundamentals of Carrier Transport* (Cambridge Univ. Press, ed. 2, 2000).
51. S. A. Maier, *Plasmonics: Fundamentals and Applications* (Springer, 2007).
52. I. P. Radko, S. I. Bozhevolnyi, G. Brucoli, L. Martín-Moreno, F. J. García-Vidal, A. Boltasseva, Efficient unidirectional ridge excitation of surface plasmons. *Opt. Express* **17**, 7228–7232 (2009). doi:10.1364/OE.17.007228 Medline
53. J. M. Montgomery, S. K. Gray, Enhancing surface plasmon polariton propagation lengths via coupling to asymmetric waveguide structures. *Phys. Rev. B* **77**, 125407 (2008). doi:10.1103/PhysRevB.77.125407
54. F. P. Incropera, D. P. Dewitt, T. Bergman, A. Lavine, *Fundamentals of Heat and Mass Transfer* (Wiley, ed. 6, 2007).

ACKNOWLEDGMENTS

The authors acknowledge fruitful discussions with Peter Nordlander, Supriyo Datta and Ravishankar Sundararaman. **Funding:** The work was supported by a grant from the Army Research Office [grant no. W911NF-19-1-0279 to P.R., V.M.S., and E.M. (design of plasmonic structures and modelling)]. P.R. and E.M. acknowledge support from the Department of Energy [DOE-BES award No. DE-SC0004871 (scanning probe measurements and analysis)], the US Office of Naval Research [ONR award No. N00014-16-1-2672 (Synthesis of ***H1***)] and from the US National Science Foundation 1803983). V.G., P.R., and E.M. thank the Department of Mechanical Engineering at the Univ. of Michigan for support via a RIP-ME grant (DFT calculations). A.B. and V.M.S. acknowledge support from Air Force Office of Scientific Research grant on Transdimensional Photonics (fabrication of ultra-thin gold films). V.G. acknowledges the support of the Army Research Office for a DURIP award (grant no. W911NF1810242), which provided the computational resources for the DFT calculations. A.V. and S.J.H acknowledge support from the EPSRC (grant no. EP/M029522/1). **Author contributions:** H.R., K.W., P.R., V.M.S., and E.M. conceived the project; H.R. and K.W. designed and developed the experimental methods under the guidance of P.R., V.M.S., and E.M.; H.R. fabricated the ultra-thin gold plasmonic structures; K.W. and H.R. conducted the single-molecule transport measurements; Z.K. performed the FDTD field profile and thermal simulations under the guidance of A.B.; L.Z. conducted the ab initio calculations on hot-carrier generation rates under the supervision of V.G.; S.Y. prepared the template stripped gold films for transmission function mapping measurements; A.V. synthesized the LUMO molecule ***L1*** under the guidance of S.J.H.; P.R., V.M.S., and E.M. supervised the project; H.R., K.W., L.Z., A.B., P.R., V.M.S., and E.M. wrote the manuscript with comments and inputs from all other authors. **Competing interests:** The authors declare no competing interests. **Data and materials availability:** All of the data pertaining to the work are available in the manuscript or the supplementary materials.

SUPPLEMENTARY MATERIALS

science.sciencemag.org/cgi/content/full/science.abb3457/DC1
Materials and Methods
Supplementary Text
Figs. S1 to S25
References (*31*–*54*)

23 February 2020; accepted 21 May 2020
Published online 4 June 2020
10.1126/science.abb3457

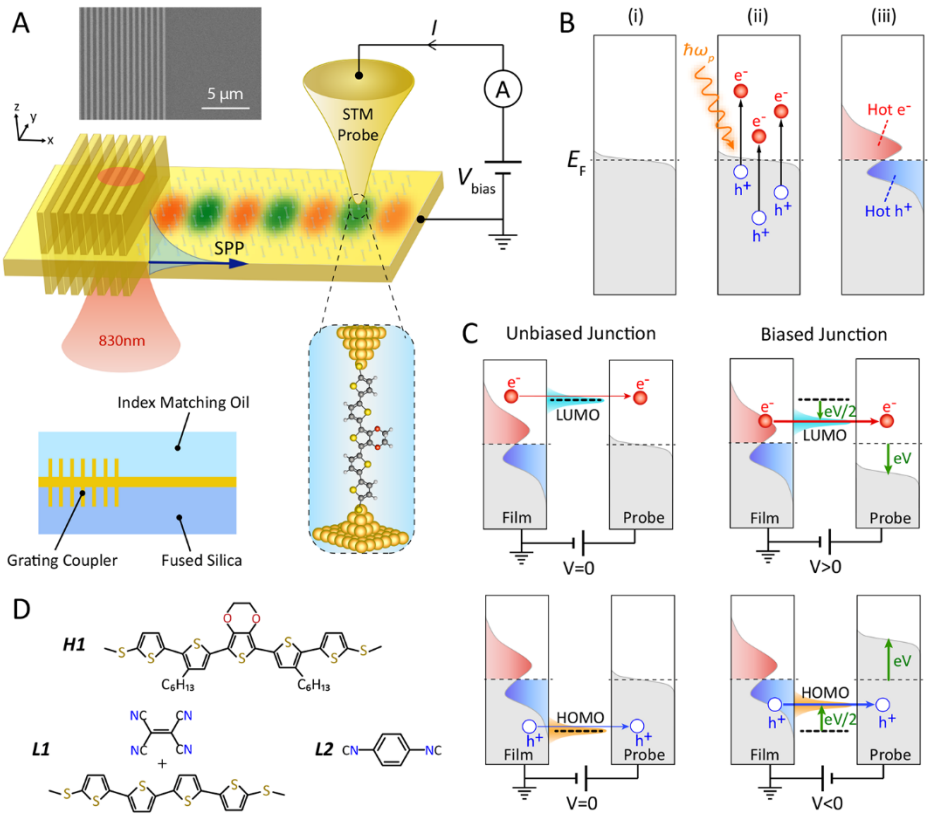

Fig. 1. Experimental setup and strategy to map hot-carrier energy distributions (HCEDs). (**A**) Schematic of the experimental set-up. SMJs are formed between a grounded nanodevice (Au film with integrated grating coupler, see electron micrograph) and a biased Au STM probe. SPPs are excited by illuminating the grating coupler with 830 nm CW laser. The bottom left graphic represents a cross-section of the nanodevice covered with index matching oil. (**B**) Schematic of hot-carrier generation. (i) Equilibrium Fermi function. (ii) Non-radiative decay of SPP energy ($\hbar\omega_p$) generates electron-hole pairs, resulting in (iii) non-equilibrium distribution of hot-electrons and holes. (**C**) Schematic showing how LUMO or HOMO-dominated SMJs with sharp transmission peaks selectively transmit hot-carriers. Biasing the junctions shifts the transmission peak with respect to the equilibrium Fermi level enabling quantification of HCED. (**D**) Structures of molecules used in this work.

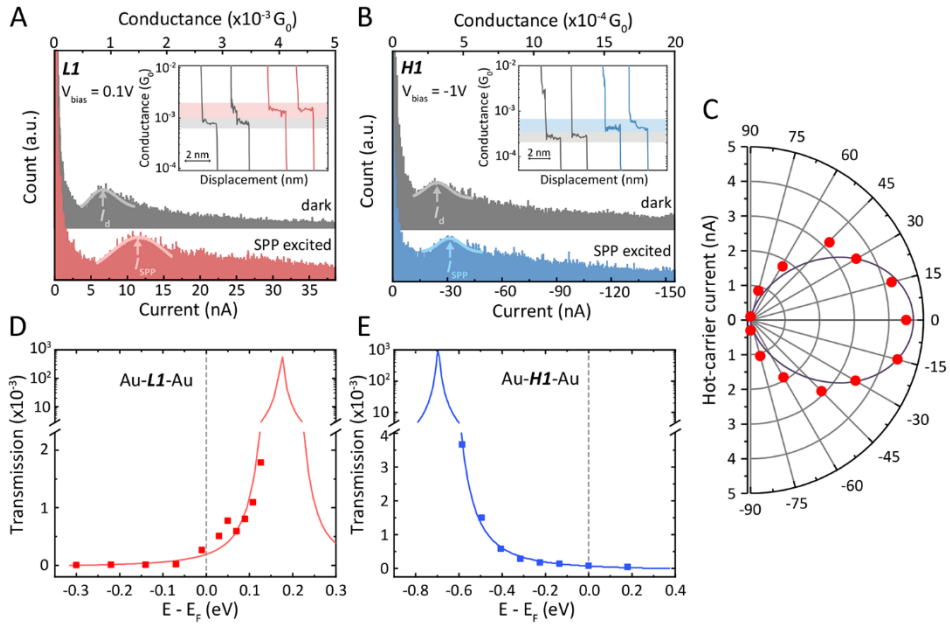

Fig. 2. Hot-carrier induced changes in SMJ currents, polarization-dependence, and transmission characteristics of *L1* and *H1* molecules. (**A**) Current and conductance histograms of Au-***L1***-Au SMJs from over 2000 traces of dark (grey) and SPP-excited (magenta) measurements at V_{bias} = 0.1 V. Gaussian fits to the histogram peaks are represented as solid lines and the vertical arrows indicate the most probable conductance and current. Inset shows representative conductance traces following the same color coding. (**B**) Same as (A), but for Au-***H1***-Au junctions and −1.0 V bias voltage. The grey and blue colors correspond to measurements from dark and SPP-excited cases, respectively. (**C**) Polarization-dependence of the hot-carrier current for Au-***L1***-Au junctions (red circles) at 0.1 V bias voltage along with the best-fit $\cos^2\theta$ dependence (black line). (**D**) and (**E**) Measured transmission functions (note the linear and logarithmic scales) of Au-***L1***-Au and Au-***H1***-Au junctions along with the Lorentzian fits (solid lines).

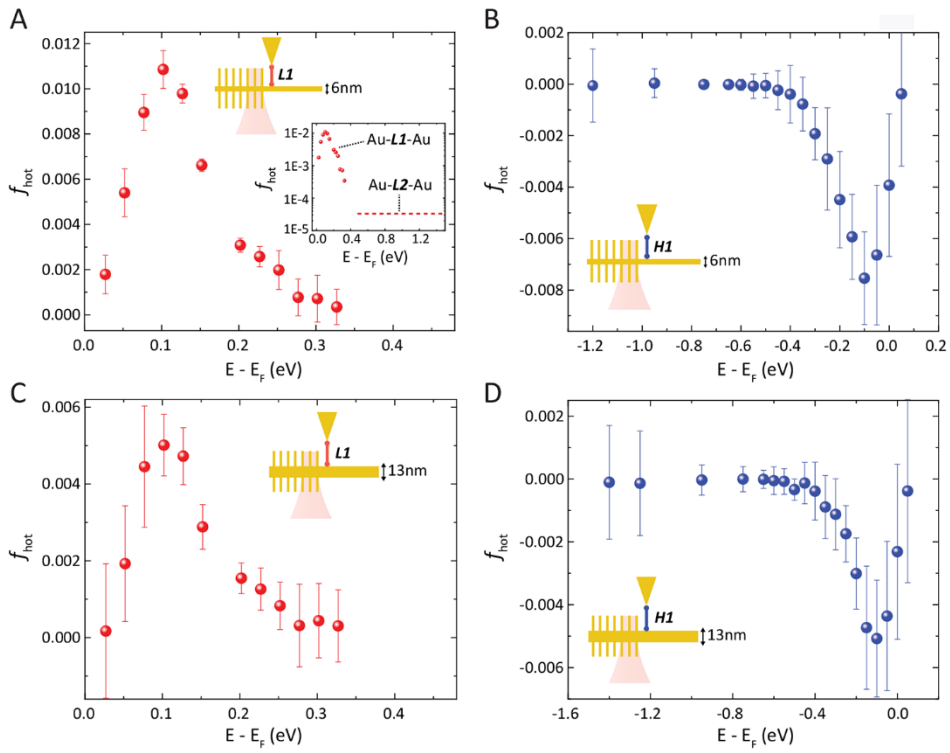

Fig. 3. Energy distributions of hot-carriers in 6 nm and 13 nm-thick Au films. (**A**) The measured HEED in a 6 nm Au film obtained from measurements on Au-*L1*-Au and Au-*L2*-Au SMJs. The energy distribution in the range up to 0.33 eV was measured with Au-*L1*-Au junctions. The inset shows the HEED on a log scale and the dashed line represents the upper bound on the average $f_{hot}(E)$ in the energy window {0.4 eV:1.45 eV} as determined with Au-*L2*-Au junctions. (**B**) The measured HHED in a 6 nm Au film using Au-*H1*-Au junctions under otherwise identical conditions compared to (A). (**C** and **D**) Measured HCEDs for 13 nm Au film but otherwise as for (A) and (B). The error bars correspond to the propagated errors from uncertainties in the measured $I_{hot}(V_{bias})$.

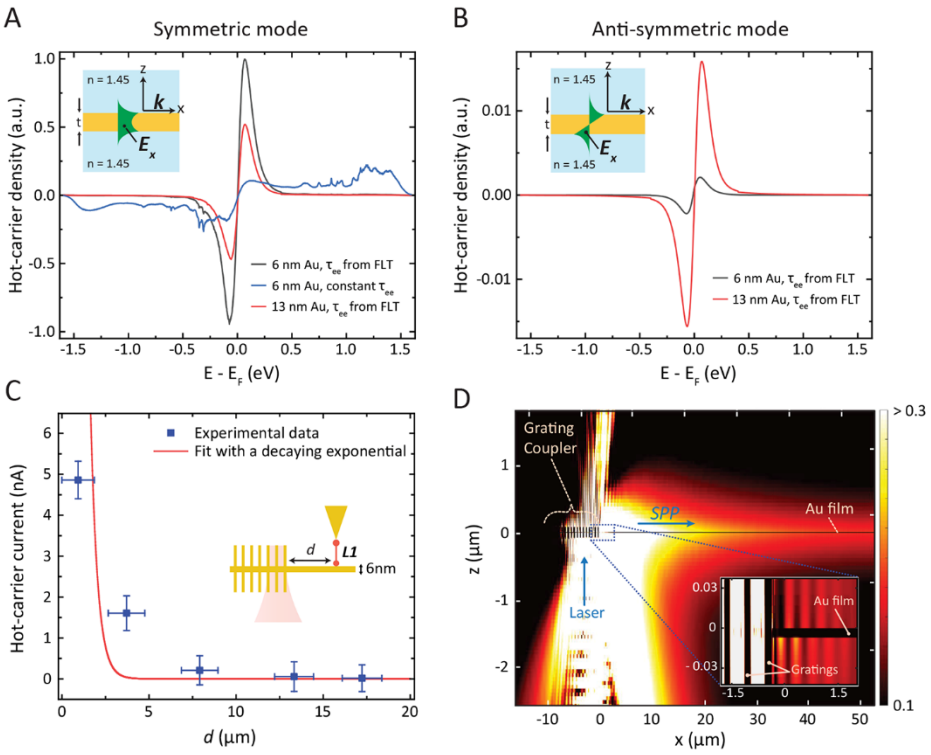

Fig. 4. Computed HCEDs, distance dependence and intensity profile. (**A**) Computed HCEDs in 6 nm- and 13 nm-thick Au films, arising from the symmetric plasmonic mode with electron-electron scattering rates from either FLT or an energy-independent scattering rate and a constant electron-phonon relaxation rate. Inset shows the employed geometry and mode profile. (**B**) Same as (A), but for the antisymmetric plasmonic mode. Note that the y-axis scale is smaller in (B) compared to (A). (**C**) Measured I_{hot} through Au-*L1*-Au SMJs (V_{bias} = 0.1 V) for varying separations *d* between the probe tip and the grating edge. Error bars represent uncertainties in *d* and I_{hot}. The red curve is an exponential fit constrained to have a decay length of 405 nm, corresponding to the symmetric mode's decay constant in 6 nm gold film [see (*20*), section 14]. (**D**) Simulated intensity profile normalized to the incident field intensity upon illuminating the gratings with a focused 830 nm laser (spot size of 5.6 μm). Inset shows the intensity profile near the grating edge. The color map of the inset is adjusted to show the beating pattern and is different from the main panel color map.

Determining plasmonic hot-carrier energy distributions via single-molecule transport measurements

Harsha Reddy, Kun Wang, Zhaxylyk Kudyshev, Linxiao Zhu, Shen Yan, Andrea Vezzoli, Simon J. Higgins, Vikram Gavini, Alexandra Boltasseva, Pramod Reddy, Vladimir M. Shalaev and Edgar Meyhofer

published online June 4, 2020